CrossMark

ORIGINAL RESEARCH

Romosozumab Treatment Converts Trabecular Rods into Trabecular Plates in Male Cynomolgus Monkeys

Jonathan B. Matheny[1,2] · Ashley M. Torres[1,2] · Michael S. Ominsky[3] · Christopher J. Hernandez[1,2,4]

Abstract Treatment with sclerostin antibody (romosozumab) increases bone formation while reducing bone resorption, leading to increases in bone volume and bone mineral density. Sclerostin antibody treatment may also provide beneficial changes in trabecular microarchitecture and strength that are not reflected in bone volume and density. Here we use three-dimensional dynamic histomorphometry to determine longitudinal changes in vertebral trabecular microarchitecture in adolescent male cynomolgus monkeys (4–5 years old) treated with sclerostin antibody. Animals were treated bi-weekly with either sclerostin antibody (30 mg/kg, sc, $n=6$) or vehicle ($n=6$) for 10 weeks. Animals were administered fluorochrome bone formation labels on days 14 and 24 (tetracycline) and on days 56 and 66 (calcein), followed by necropsy on day 70. Cylindrical specimens of cancellous bone from the 5th lumbar vertebrae were used to generate high-resolution, three-dimensional images of bone and fluorescent labels of bone formation ($0.7 \times 0.7 \times 5.0$ μm/voxel). The three-dimensional images of the bone formation labels were used to determine the bone volume formed between days 14 and 66 and the

resulting alterations in trabecular microarchitecture within each bone. Treatment with sclerostin antibody resulted in a conversion of rod-like trabeculae into plate-like trabeculae at a higher rate than in vehicle-treated animals ($p=0.01$). Plate bone volume fraction was greater in the sclerostin antibody group relative to vehicle (mean 43 vs. 30%, $p<0.05$). Bone formation increased the thickness of trabeculae in all three trabecular orientations (axial, oblique, and transverse, $p<0.05$). The volume of bone formed between days 14 to 66 was greater in sclerostin antibody-treated groups (9.0 vs. 5.4%, $p=0.02$), and new bone formation due to sclerostin antibody treatment was associated with increased apparent stiffness as determined from finite element models. Our results demonstrate that increased bone formation associated with sclerostin antibody treatment increases plate-like trabecular morphology and improves mechanical performance.

Electronic supplementary material The online version of this article (doi:10.1007/s00223-017-0258-3) contains supplementary material, which is available to authorized users.

✉ Christopher J. Hernandez
cjh275@cornell.edu

1 Sibley School of Mechanical and Aerospace Engineering, Cornell University, 355 Upson Hall, Ithaca, NY 14853, USA

2 Department of Biomedical Engineering, Cornell University, Ithaca, NY, USA

3 Department of Cardiometabolic Disorders, Amgen Inc., Thousand Oaks, CA, USA

4 Hospital for Special Surgery, New York, NY, USA

Introduction

Osteoporosis is characterized by deterioration of cancellous bone microstructure, including reductions in bone volume fraction and trabecular thickness [1]. Anabolic treatments for osteoporosis have the potential to reverse bone loss and recover trabecular microstructure by causing increases in new bone formation. Romosozumab is an antibody that blocks sclerostin, a protein secreted by osteocytes that negatively regulates bone formation [2–6]. Animal studies have shown that sclerostin antibody treatment increases modeling-based bone formation while reducing bone resorption [7] leading to increases in bone mass and bone strength

[2, 8]. Recent clinical studies have shown that sclerostin antibody treatment increases bone mineral density in the lumbar spine and hip [9–11] and reduces vertebral fracture risk in postmenopausal women [12]. Although increases in bone mineral density often result in increases in bone strength and resistance to fracture, many osteoporosis treatments cause reductions in fracture risk that are greater than expected from changes in bone mineral density alone [13, 14]. Possible explanations for the disproportionate change in fracture risk include alterations in bone tissue mechanical properties, cortical-trabecular density distribution, and cancellous bone microarchitecture [15].

Cancellous bone microarchitecture is an aspect of bone quality that may influence fracture risk [15]. Traditional measures of cancellous bone microarchitecture include bone volume fraction, average trabecular thickness, and trabecular separation [16]. However, direct enumeration and classification of individual trabeculae through individual trabecula segmentation (ITS) has been shown to improve the prediction of cancellous bone strength and stiffness beyond what is possible with traditional measures [17–19]. Additionally, alterations in rod- and plate-like morphology of cancellous bone in patients has been associated with fragility fractures independent of bone mineral density determined through dual-energy X-ray absorptiometry [20]. Hence, changes in rod-like and plate-like trabecular microarchitecture have the potential to improve bone mechanical performance to a greater extent than expected from bone mineral density.

While anabolic treatments clearly increase bone volume fraction, they may also influence aspects of cancellous microstructure that influence bone quality. The number and orientation of trabeculae are known to influence biomechanical performance of cancellous bone. It is believed that once a trabecula is resorbed during age-related bone loss, it cannot be reformed by subsequent bone formation and that subsequent increases in bone density occur through thickening of existing trabeculae [21]. Finite element models suggest that increasing the number of trabeculae is more effective at increasing cancellous bone strength and stiffness than thickening existing trabeculae [21]. Differentiating between increases in the number and thickness of trabeculae is challenging because bone formation is typically assessed in two-dimensional sections which do not display out-of-plane morphology, making it difficult to identify the presence of entirely new trabeculae [22, 23]. Three-dimensional imaging using in vivo, serial micro-computed tomography (serial micro-CT) [24–29] or high-resolution peripheral quantitative computed tomography (HR-pQCT) [30–33] has been used to evaluate changes in cancellous bone microarchitecture due to bone formation; however, both approaches have limited spatial resolution (10.5 μm for serial micro-CT and 82 μm or higher for HR-pQCT)

and have typically been used only to study extremities. We have demonstrated a three-dimensional dynamic histomorphometry approach that provides assessment of bone formation markers in vitro [34–37], allowing for examination of changes in trabecular microarchitecture caused by bone formation that can be used on specimens from any region of the skeleton.

While cross-sectional studies have associated sclerostin antibody treatment with increased bone volume fraction [2, 7, 8, 38], there are no longitudinal studies of alterations in trabecular microarchitecture in the spine. It is not known how treatment with sclerostin antibody alters the rod and plate-like morphology of individual trabeculae in cancellous bone. Given the anabolic nature of sclerostin antibody, we hypothesize that treatment will generate sufficient bone formation to increase the total number of trabeculae or specifically increase the number of plate-like trabeculae. The long-term goal of the current line of investigation is to understand how changes in bone formation and microarchitecture influence cancellous bone biomechanics and fracture risk. In the current study, we combine individual trabecula segmentation with three-dimensional dynamic bone histomorphometry to determine the changes in the number and size of rod-like and plate-like trabeculae in vertebral cancellous bone over an 8-week period of treatment with sclerostin antibody.
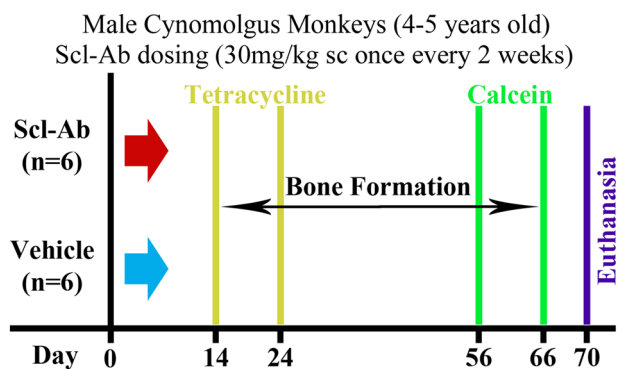
Materials and Methods

Study Design

Here we report a new analysis using tissue generated from a prior study. The study was performed under Institutional Animal Care and Use Committee approval at Charles River Laboratories (Montreal, Quebec, Canada), which has been thoroughly described elsewhere [7, 38]. All efforts were made to minimize animal suffering. Adolescent (4–5 year old) male cynomolgus monkeys (Macaca fascicularis) were used in the study because the monoclonal antibody (romosozumab) can only be used effectively in humans or primates. The animals were cared for in accordance to the Guide for the Care and Use of Laboratory Animals, and were maintained in Association for Assessment and Accreditation of Laboratory Animal Care International—accredited facilities in species-specific housing on a 12:12 h light:dark cycle. The animals were socially housed indoors in environmental conditions $24 \pm 3\,°C$, $50 \pm 20\%$ humidity and were allowed normal physical activity. Animals were fed twice daily a certified pelleted primate diet (2050 °C Certified Global 20% Protein Primate Diet: Harlan Teklad) in amounts appropriate for the age and size of the animals. In addition, each animal was offered food

supplements daily in any combination of the following: Golden Banana Softy®, Prima-Treat® (5 g format), fresh or dried fruit, fresh or dried vegetables, and at least once weekly Prima-Foraging Crumbles® (20–25 g) as part of the environmental enrichment program. Animals had ad libitum access to water that was treated by reverse osmosis and ultraviolet radiation.

The cynomolgus monkeys were randomly assigned to receive either sclerostin antibody (Scl-Ab, 30 mg/kg romosozumab, subcutaneous injection, $n = 6$) or vehicle (10 mM sodium acetate, 9% sucrose, 0.004% polysorbate 20, pH 5.2, $n = 6$) bi-weekly for 10 weeks. Animals received fluorochrome labels on days 14 and 24 (25 mg/kg tetracycline, intravenous) and on days 56 and 66 (8 mg/kg calcein, intravenous) following treatment. Romosozumab was well tolerated by the animals, and no adverse effects of sclerostin inhibition were observed. Following administration of a sedative (ketamine, intramuscular injection), monkeys were euthanized by intravenous injection of sodium pentobarbital followed by exsanguination by incision of the axillary or femoral arteries (see Fig. 1). The fifth lumbar vertebra was stored at −20 °C.

Image Acquisition and Processing

Cylindrical specimens of cancellous bone (4 mm in height, 5 mm diameter) were obtained from the center of the 5th lumbar vertebral body. Bone marrow was removed from the specimens using a low-pressure water jet, and specimens were embedded undecalcified in methylmethacrylate. Three-dimensional images of bone and fluorochrome labels were obtained using serial milling (voxel size of $0.7 \times 0.7 \times 5.0$ μm) as described previously (see Fig. 2) [34–36]. Serial milling uses a custom-made

Male Cynomolgus Monkeys (4-5 years old)
Scl-Ab dosing (30mg/kg sc once every 2 weeks)

Fig. 1 The timing of treatment and fluorochrome labeling in the study design are illustrated. Male cynomolgus monkeys were administered either sclerostin antibody (Scl-Ab, $n = 6$) or vehicle. Animals received fluorochrome labels on days 14 and 24 (tetracycline) and on days 56 and 66 (calcein) following treatment, and were euthanized at day 70

system that involves repeatedly removing the top 5 μm from the specimen using a computer-controlled milling system (Benchman MX, Intelitek, Manchester, NH, USA) and collecting a mosaic of images from the newly revealed block face using epifluorescence microscopy. Three fluorescent images were collected of each cross-section using different filter sets: one for bone autofluorescence (390/460 nm Ex/Em), one for tetracycline labels (390/630 nm), and one for calcein labels (480/535 nm). A manually determined global threshold was selected by a trained observer to segment bone and fluorescent labels (tetracycline and calcein). The segmentation approach has been shown to provide similar results as two-dimensional histomorphometry measurements with low interobserver variation [34]. A cylindrical region of interest of 2 mm in height, 4 mm in diameter from the center of each specimen was used for analysis.

Three-Dimensional Measurements of Bone Formation

Three-dimensional dynamic bone histomorphometry differs from traditional dynamic histomorphometry in that it measures bone formation throughout the specimen and is therefore not subject to limitations associated with stereology or "label escape error," making it possible to evaluate changes in bone formation in a region of cancellous bone and longitudinal assessment of changes in bone microstructure caused by bone formation. Three-dimensional measures of bone formation were generated from the images using measurement approaches described previously [34]. Three-dimensional mineral apposition rate (3D MAR) and mineralizing surface (3D MS/BS) were determined for each of the two pairs of fluorescent labels (one pair of tetracycline and one pair of calcein) [34]. Three-dimensional bone formation rate was calculated as the mineral apposition rate multiplied by the mineralizing surface (3D BFR/BS-Tet and 3D BFR/BS-Cal). In addition to determining the bone formation indices of each of the two pairs of fluorescent labels, the entire volume of bone formed between the administration of the first tetracycline label (day 14) and the last calcein label (day 66), and the bone formed between the last calcein label and euthanasia (day 70) was determined by merging all of the fluorescent labels and the adjacent surface in the three-dimensional image using morphological closing. The resulting volume was referred to as the Formation Volume (FV) and represents a direct measure of the entire volume of bone formed during the 8-week period between first and last formation labels (Fig. 2). The changes in trabecular microarchitecture between images with and without the formation volume therefore approximated longitudinal changes in trabecular morphology.
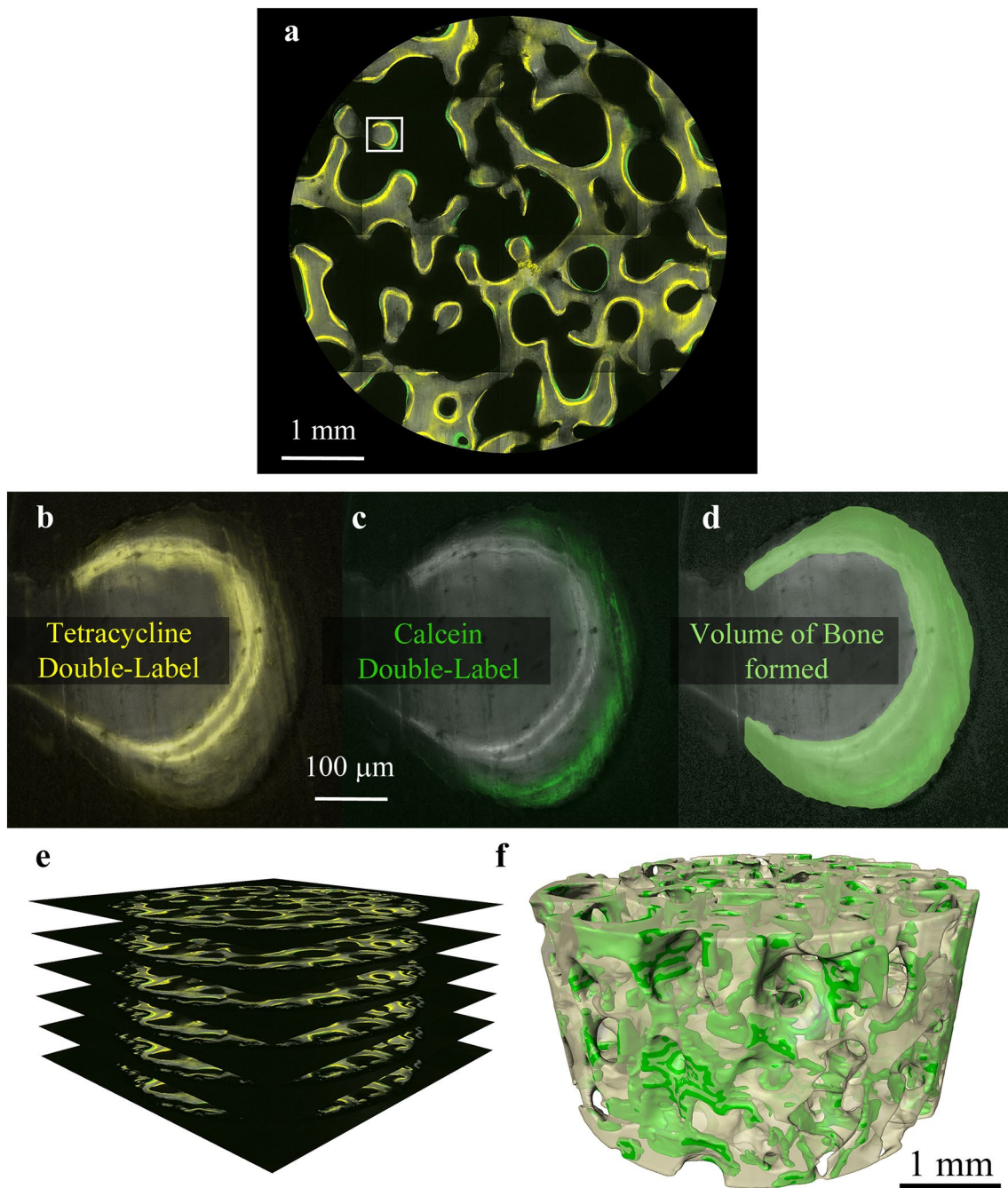
Fig. 2 **a** A representative cross-section from a cancellous bone specimen with bone and fluorescent formation markers (*tetracycline yellow* (**b**) and *calcein green* (**c**)) was obtained using serial milling at a voxel size of $0.7 \times 0.7 \times 5.0$ μm. The two pairs of bone formation labels were merged using three-dimensional morphological closing to isolate the Formation Volume (**d**).Three-dimensional images of bone and bone formation were created from the collection of two-dimensional cross-sections (formation volume shown in *green*) (**e–f**). (Color figure online)

Individual Trabecula Segmentation-Based Analyses

The morphology of individual trabeculae was analyzed using individual trabecula segmentation (ITS, Columbia University). Images were coarsened to $21 \times 21 \times 21$ μm voxels to reduce computational time and to provide measures consistent with prior work [17]. Individual trabecula segmentation associates each voxel of bone in the image with a discrete trabecula and then characterizes the trabecular morphology (rod-like, plate-like) and orientation (axial, oblique, and transverse, see Fig. 3) (Please see [17] for further details). The plate bone

Fig. 3 Three-dimensional images of bone formation and local trabecular morphology and orientation are shown for each group. Cancellous bone specimens from the 5th lumbar vertebra for each group are shown for **a** bone formation volume **b** plate-like and rod-like trabecular microstructure and **c** trabecular orientation for each group
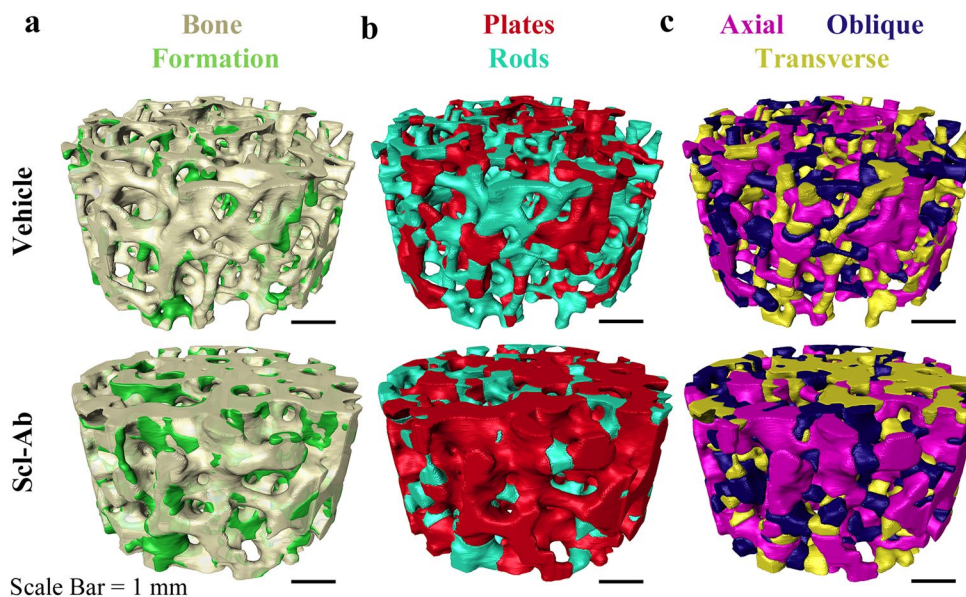
volume fraction (pBV/TV) and rod bone volume fraction (rBV/TV) were measured for each group along with measurements of volume fraction and trabecular thickness for each trabecular orientation (axial, oblique, and transverse). To determine the longitudinal changes in rod-like and plate-like morphology and trabecular orientation caused by bone formation during the experiment, ITS was performed on the final images as well as the same images after removal of the formation volume. The number of trabeculae that were changed from rod-like to plate-like as a result of bone formation during the 8-week period of the experiment was then determined. Extensive analysis for entirely new trabeculae formed between the first and last formation labels was performed. Traditional three-dimensional measurements of bone (bone volume fraction (BV/TV), trabecular thickness (Tb.Th.), trabecular separation (Tb.Sp.), and structure model index (SMI) were measured using BoneJ [39].

Serum Markers of Bone Formation

Serum osteocalcin (OC) and intact N-terminal propeptide of type 1 procollagen (P1NP), markers of bone formation, were measured using radioimmunoassay (OC: DSL-6900, Diagnostic System Laboratories country; P1NP: Intact P1NP, Orion Diagnostica) at various time points, with the day 14 time point corresponding to the initial fluorochrome label utilized for regression analysis. Please see Ominsky et al. for a full description of experimental procedures [8, 38] .

Finite Element Analysis

Linear elastic finite element models were created from three-dimensional images of the cancellous bone specimens (21-µm voxels) with and without the bone formed during the 8 weeks between formation labels. Each finite element model consisted of 0.62–1.69 million elements. Bone tissue was assumed to be an isotropic, linear elastic material with Young's modulus 10 GPa and Poisson's ratio of 0.3. To determine axial stiffness, an apparent compressive strain of 1% was applied to the top surface in the axial direction (Z-axis), and vertical displacement on the opposite surface was fixed. To determine transverse stiffness, a cubic region of interest 2 mm in size was taken from the center of each specimen, and finite element models were created with displacement applied in the transverse direction (Y-axis). Apparent stress was calculated from the sum of the reaction forces on the constrained surface divided by the cross-sectional area of the surface. Apparent stiffness was calculated as the apparent stress divided by the applied apparent strain. Finite element models were implemented using Abaqus (Abaqus 6.9, Dassault Systèmes, Velizy-Villacoublay, France) with the Abaqus/Standard solver.

Statistical Analyses

Differences in three-dimensional measurements of bone formation, bone microarchitecture, and ITS-based measurements between vehicle- and sclerostin antibody-treated groups were identified using two-tailed t-tests with JMP (JMP Pro 10.0.2, SAS Institute Inc., Cary, NC, USA). In addition, linear regression analyses were performed with
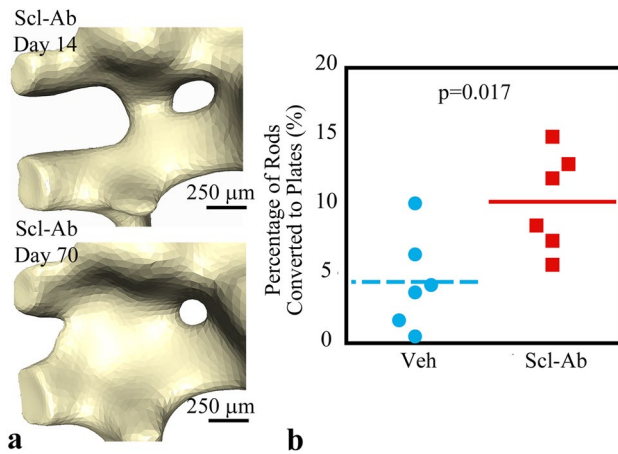
JMP. A p-value of 0.05 was used to determine statistical significance.

Results

Over the 8-week period of the study, more rod-like trabeculae were converted to plate-like trabeculae in animals treated with sclerostin antibody ($10.27 \pm 3.59\%$,


Fig. 4 Sclerostin antibody converts trabecular rods to trabecular plates. **a** An example of the conversion of rod-like trabeculae to a plate-like trabecula is shown (sclerostin antibody-treated animal). **b** The percentage of rod-like trabeculae which were converted to plate-like trabeculae during the 8-week study period is shown

mean $\pm$ SD) than in vehicle-treated animals ($4.45 \pm 3.48\%$, $p = 0.017$, see Fig. 4; Table 1). The volume of bone formed over the 8-week study period (Formation Volume) was 68% greater in sclerostin antibody-treated animals as compared to vehicle controls ($p = 0.015$, see Fig. 5a; Table 2). The increase in newly formed bone volume was achieved by an increase in bone formation rate (3D BFR/BS, $p = 0.001$) (see Fig. 5b; Table 2). The increases in 3D MAR, 3D MS/BS, and 3D BFR/BS due to sclerostin antibody treatment early in the study (days 14–24 observed with tetracycline) was similar to that later in the study (days 56–66, observed with calcein, Table 2). Additionally, serum markers of bone formation (OC and P1NP) measured in 2 weeks following treatment were strongly correlated with the three-dimensional bone formation rate (see Fig. 5c–d). Extensive examination of the specimens failed to provide evidence of the formation of entirely new trabeculae.

Sclerostin antibody treatment was associated with large changes in trabecular rod- and plate-like morphology, including increases in the plate bone volume fraction ($p < 0.045$, see Fig. 6a; Table 1). Additionally, sclerostin antibody treatment increased the thickness of both plate-like and rod-like trabeculae compared to controls ($p < 0.05$, Table 1). Increases in trabecular thickness associated with sclerostin treatment were distributed uniformly among trabeculae with different orientation (axial, oblique, and transverse) ($p < 0.05$, see Fig. 6b; Table 1). Additional ITS-based microstructural measurements can be found in Online Resource 1.

Table 1 Traditional and ITS-based bone microstructural measurements are shown for each group, Mean $\pm$ SD, 95% CI (5th, 95th)

Measurement	Vehicle ($n = 6$)	Scl-Ab ($n = 6$)	p-value
Bone volume fraction (BV/TV, %)	42.10 ± 12.14 (29.37, 54.84)	53.87 ± 4.68 (48.96, 58.78)	0.051
Trabecular thickness (Tb.Th, μm)	219.18 ± 42.35 (174.74, 263.63)	272.39 ± 33.66 (237.06, 307.71)	0.037
Structural modeling index (SMI)	0.99 ± 0.82 (0.13, 1.85)	0.13 ± 0.47 (−0.36, 0.62)	0.050
Trabecular separation (Tb.Sp, μm)	679.97 ± 32.94 (645.40, 714.54)	687.12 ± 29.95 (655.69, 718.55)	0.702
Plate bone volume fraction (pBV/TV, %)	30.08 ± 12.90 (16.55, 43.61)	42.88 ± 4.67 (37.98, 47.78)	0.045
Rod bone volume fraction (rBV/TV, %)	12.31 ± 3.38 (8.76, 15.86)	11.41 ± 3.30 (7.94, 14.88)	0.650
Plate volume/bone volume (pBV/BV, %)	69.00 ± 12.55 (56.45, 81.55)	79.63 ± 5.97 (73.65, 85.60)	0.091
Plate bone volume /rod bone volume (pBV/rBV)	2.66 ± 1.53 (1.06, 4.27)	4.06 ± 1.33 (2.67, 5.46)	0.121
Plate-like trabecular thickness (pTb.Th, μm)	194.15 ± 36.90 (155.43, 232.87)	239.33 ± 27.29 (210.70, 267.96)	0.037
Rod-like trabecular thickness (rTb.Th, μm)	153.92 ± 7.74 (145.79, 162.05)	166.66 ± 8.99 (157.23, 176.09)	0.025
No. of rods converted to plates/no. rods (%)	4.45 ± 3.48 (0.80, 8.10)	10.27 ± 3.59 (6.50, 14.05)	0.017
Axial-bone volume fraction (aBV/TV, %)	19.12 ± 6.24 (12.62, 25.72)	26.32 ± 2.66 (23.54, 29.12)	0.026
Oblique-bone volume fraction (oBV/TV, %)	11.97 ± 3.46 (8.33, 15.60)	15.13 ± 2.20 (12.82, 17.45)	0.088
Transverse-bone volume fraction (tBV/TV, %)	11.34 ± 3.23 (7.95, 14.73)	12.87 ± 2.75 (9.99, 15.76)	0.396
Axial-trabecular thickness (aTb.Th, μm)	225.02 ± 41.27 (181.71, 268.32)	273.62 ± 32.71 (239.30, 307.94)	0.047
Oblique-trabecular thickness (oTb.Th, μm)	229.04 ± 46.20 (180.55, 277.52)	285.26 ± 37.18 (246.23, 324.28)	0.043
Transverse-trabecular thickness (tTb.Th, μm)	224.70 ± 42.00 (180.62, 268.77)	283.83 ± 36.17 (245.87, 321.78)	0.026
Axial apparent stiffness (MPa)	2270 ± 1113 (1102, 3438)	3327 ± 416 (2891, 3764)	0.054
Transverse apparent stiffness (MPa)	1464 ± 852 (570, 2358)	2401 ± 439 (1940, 2862)	0.038

Fig. 5 Sclerostin antibody increases three-dimensional bone formation related to serum markers of bone formation. Three-dimensional measurements of bone formation are shown for each group **a** Newly formed bone volume, **b** bone formation rate. Percentage change in **c** serum osteocalcin (OC) and (**d**) and serum intact N-terminal propeptide of type 1 procollagen (P1NP) as measured 2 weeks following treatment and compared to baseline levels (week 0) correspond to the three-dimensional bone formation rate
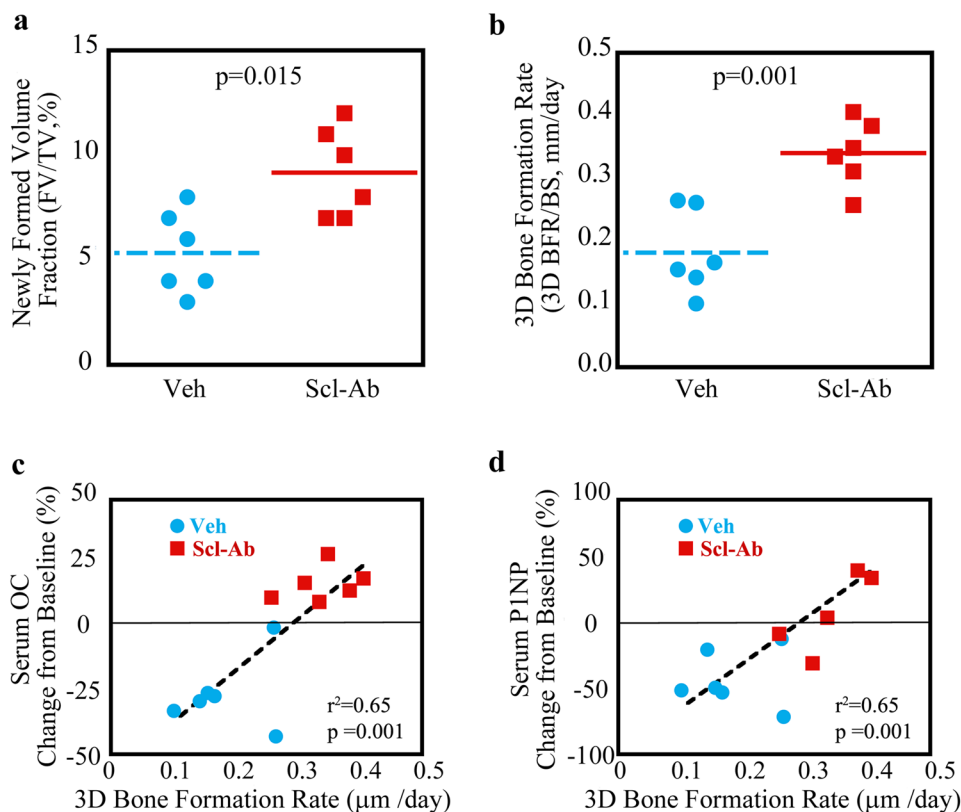

Table 2 Three-dimensional dynamic bone histomorphometry measurements are shown for each group, Mean ± SD, 95% CI (5th, 95th)

Measurement	Vehicle (*n* = 6)	Scl-Ab (*n* = 6)	*p*-value
Newly formed volume fraction (FV/TV, %)	5.38 ± 2.04 (3.24, 7.53)	9.04 ± 2.28 (6.65, 11.44)	0.015
3D mineralizing surface (3D MS/BS, %)	26.30 ± 8.80 (17.07, 35.53)	40.35 ± 5.07 (35.03, 45.67)	0.007
3D mineral apposition rate (3D MAR, μm/day)	0.69 ± 0.05 (0.63, 0.74)	0.84 ± 0.05 (0.79, 0.89)	0.0003
3D bone formation rate (3D BFR/BS, μm/day)	0.18 ± 0.07 (0.11, 0.25)	0.34 ± 0.05 (0.29, 0.39)	0.001
3D mineralizing surface-tetracycline labels (3D MS/BS-Tet, %)	14.10 ± 10.82 (2.74, 25.46)	33.32 ± 9.77 (23.07, 43.58)	0.009
3D Mineral apposition rate-tetracycline labels (3D MAR-Tet, μm/day)	1.45 ± 0.19 (1.25, 1.65)	1.55 ± 0.07 (1.48, 1.63)	0.260
3D bone formation rate-tetracycline labels (3D BFR/BS-Tet, μm/day)	0.22 ± 0.19 (0.02, 0.42)	0.52 ± 0.17 (0.34, 0.70)	0.016
3D mineralizing surface-calcein labels (3D MS/BS-Cal, %)	12.32 ± 7.49 (4.46, 20.19)	34.40 ± 9.29 (24.65, 44.15)	0.001
3D mineral apposition rate-calcein labels (3D MAR-Cal, μm/day)	1.42 ± 0.18 (1.23, 1.60)	1.63 ± 0.12 (1.50, 1.75)	0.038
3D bone formation rate-calcein labels (3D BFR/BS-Cal, μm/day)	0.17 ± 0.10 (0.07, 0.27)	0.56 ± 0.16 (0.39, 0.72)	0.0004

Sclerostin antibody treatment increased apparent stiffness in the axial and transverse directions compared to vehicle controls ($p = 0.038$–0.054; Table 1). Apparent stiffness in both directions was strongly correlated with measurements of cancellous bone microarchitecture such as bone volume fraction, plate bone volume fraction, and axial-bone volume fraction (see Online Resource 2).

Discussion

Over an 8-week period, treatment with sclerostin antibody increased bone formation leading to a conversion of rod-like trabeculae to plate-like trabeculae and an increase in thickness of trabecular plates and rods in cancellous bone. Trabecular orientation did not influence where sclerostin
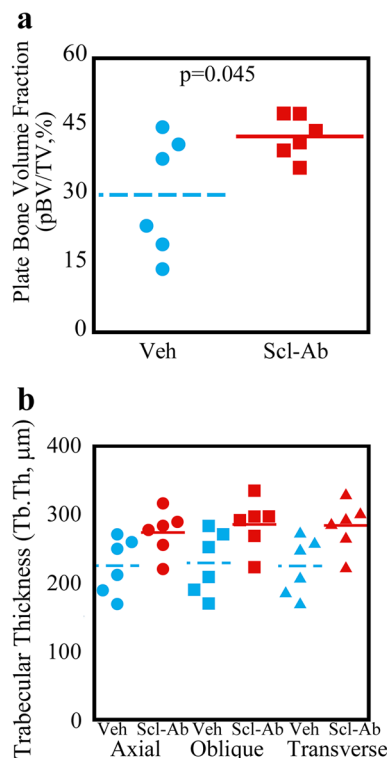
Fig. 6 Sclerostin antibody treatment improves trabecular morphology and orientation. **a** Whole specimen measurements of plate bone volume fraction are shown for each group. **b** Trabecular thickness was increased in all trabecular orientations due to sclerostin antibody treatment ($p < 0.05$ vs. Veh for each orientation)

antibody-induced bone formation occurred. Bone volume fraction correlated strongly with mechanical performance in our high-resolution finite element models, regardless of treatment condition. No measurements of local trabecular morphology or orientation imparted any additional improvements to prediction of cancellous bone mechanical performance beyond what could be attributed to bone volume fraction.

We did not observe the formation of entirely newly trabeculae in any of the specimens. Banse and colleagues observed new trabecular connections, or "bridges" in two-dimensional, backscatter electron microscopy images. Banse surmised that these bridges were repairing struts perforated by osteoclastic resorption [22, 23]. In analyzing trabecular bone in three dimensions, we observed multiple cross-sectional images of trabecular bridges that were not in fact newly formed trabeculae. That no newly formed trabeculae were observed in cancellous bone with enhanced bone formation supports the idea that fenestration and loss of trabeculae during remodeling is irreversible [21].

The current study was able to analyze the rod-like and plate-like structure of individual trabeculae, providing the most detailed description of changes in trabecular

morphology associated with treatment to date. The ITS analysis is more representative of trabecular microstructure than traditional measures such as SMI, which measures rod- and plate-like trabecular morphology based solely on strut curvature. Salmon and colleagues argue that the SMI measurement is confounded by a strong correlation with bone volume fraction and, consequently, does not in fact measure the rod- and plate-like structure of trabecular bone [40]. Our findings are consistent with a report by Maquer and colleagues in which bone volume fraction and fabric anisotropy explained mechanical stiffness of cancellous bone and that morphological measurements from either individual trabecula segmentation or trabecular bone score provided no improvement in predicting cancellous bone stiffness [41].

The current study demonstrates a new method of analyzing longitudinal changes in trabecular microarchitecture associated with bone formation. Longitudinal evaluation of changes in trabecular microarchitecture has been performed with repeated, or "serial," micro-computed tomography applied to live animals [24–29]. Altman and colleagues showed that bone formation due to combined parathyroid hormone and alendronate treatment increased plate-like trabecular microarchitecture in rats over 12 days of treatment [24]. Lambers and colleagues used serial micro-computed tomography to observe changes in bone formation and resorption due to cyclic mechanical loading in a mouse-tail loading model [29]. Christen and colleagues have correlated bone formation and resorption measured using HR-pQCT with locations of physiological tissue loading in the human distal tibia. While serial micro-computed tomography and HR-pQCT are non-invasive and non-destructive methods to access remodeling sites in cancellous bone, both approaches are subject to limitations. In vivo, serial micro-CT approaches are unable to accurately capture small bone formation events due to voxel size (10–11 μm) and are limited to the extremities of small animal species. HR-pQCT allows for the imaging of human bone tissue but is even more limited to in capturing bone formation due to a voxel size (often 82 μm or greater). In contrast, longitudinal imaging of bone formation using serial milling, while time intensive, can be performed on a specimen from any skeletal site and has a voxel size of 1–5 μm allowing for the detection of small or newly initiated locations of bone formation. Additionally, serial milling involves visualization of bone formation using fluorochrome labels (the gold standard for assessment of bone formation) making it more sensitive to bone formation in cancellous bone than in vivo micro-CT or HR-pQCT, which may present errors due to partial volume effects at bone surfaces [28]. We confirmed the validity of our three-dimensional measurements by comparing them to whole system markers

for bone formation. Serum markers for bone formation (OC and P1NP) were strongly correlated with the three-dimensional dynamic bone histomorphometry ($r^2 = 0.65$ for both, Fig. 5c–d). Correlations between three-dimensional measurements of bone formation and serum markers are similar, and in some cases stronger, to correlations between two-dimensional images of fluorochrome labels and serum markers of bone formation [8, 42].

An important limitation of the current study is that we do not account for resorption that occurred during the 8-week period, resulting in slight changes to the initial trabecular microstructure. We expect that not accounting for resorption volume may explain why the percentage of rods converted to plates in vehicle controls was greater than zero, which would be expected following balanced bone remodeling. Sclerostin antibody treatment increases modeling-based formation (bone formation not preceded by bone resorption) and reduces bone resorption [7] so any effects of resorption would be minimal. A previous study using these animals has shown that alterations in bone formation and resorption due to sclerostin antibody treatment did not change bone matrix quality in comparison to vehicle controls [43]. An additional limitation of the current study is that our analysis was limited to the 5th lumbar vertebra. Although we did not examine other regions of the skeleton, a previous study found that treatment with sclerostin antibody increased bone formation (bone formation rate) as well as trabecular microstructure (trabecular thickness) in both the proximal tibia and second lumbar vertebra in adolescent female cynomolgus monkeys [8], suggesting that our findings may be indicative of changes elsewhere in the skeleton.

In conclusion, sclerostin antibody improved the trabecular morphology of cancellous bone by a prolonged increase in bone formation over 8 weeks. Improvements in local trabecular morphology due to sclerostin antibody may counteract the reduction in plate-like bone volume associated with osteoporosis.

Compliance with Ethical Standards

Conflicts of interest Michael Ominsky reports personal fees from Amgen Inc during the conduct of the study; personal fees from Amgen Inc outside the submitted work. Jonathan Matheny and Ashley Torres report non-financial support from Amgen Inc, and UCB Pharma (supplied specimens) during the conduct of the study. Christopher Hernandez reports grants and non-financial support from Amgen Inc and UCB Pharma (supplied specimens) during the conduct of the study. The authors have full control of primary data and agree to journal review of the data if requested.

Ethical Approval All applicable international, national, and/or institutional guidelines for the care and use of animals were followed. All procedures performed in studies involving animals were in accordance with the ethical standards of the institution or practice at which the studies were conducted.

References

1. Genant HK, Delmas PD, Chen P, Jiang Y, Eriksen EF, Dalsky GP, Marcus R, San Martin J (2007) Severity of vertebral fracture reflects deterioration of bone microarchitecture. Osteoporos Int 18:69–76
2. Li X, Ominsky MS, Warmington KS, Morony S, Gong J, Cao J, Gao Y, Shalhoub V, Tipton B, Haldankar R, Chen Q, Winters A, Boone T, Geng Z, Niu QT, Ke HZ, Kostenuik PJ, Simonet WS, Lacey DL, Paszty C (2009) Sclerostin antibody treatment increases bone formation, bone mass, and bone strength in a rat model of postmenopausal osteoporosis. J Bone Miner Res 24:578–588
3. Poole KE, van Bezooijen RL, Loveridge N, Hamersma H, Papapoulos SE, Lowik CW, Reeve J (2005) Sclerostin is a delayed secreted product of osteocytes that inhibits bone formation. Faseb J 19:1842–1844
4. Hamersma H, Gardner J, Beighton P (2003) The natural history of sclerosteosis. Clin Genet 63:192–197
5. Brunkow ME, Gardner JC, Van Ness J, Paeper BW, Kovacevich BR, Proll S, Skonier JE, Zhao L, Sabo PJ, Fu Y, Alisch RS, Gillett L, Colbert T, Tacconi P, Galas D, Hamersma H, Beighton P, Mulligan J (2001) Bone dysplasia sclerosteosis results from loss of the SOST gene product, a novel cystine knot-containing protein. Am J Hum Genet 68:577–589
6. Balemans W, Ebeling M, Patel N, Van Hul E, Olson P, Dioszegi M, Lacza C, Wuyts W, Van Den Ende J, Willems P, Paes-Alves AF, Hill S, Bueno M, Ramos FJ, Tacconi P, Dikkers FG, Stratakis C, Lindpaintner K, Vickery B, Foernzler D, Van Hul W (2001) Increased bone density in sclerosteosis is due to the deficiency of a novel secreted protein (SOST). Hum Mol Genet 10:537–543
7. Ominsky MS, Niu QT, Li C, Li X, Ke HZ (2014) Tissue-level mechanisms responsible for the increase in bone formation and bone volume by sclerostin antibody. J Bone Miner Res 29:1424–1430
8. Ominsky MS, Vlasseros F, Jolette J, Smith SY, Stouch B, Doellgast G, Gong J, Gao Y, Cao J, Graham K, Tipton B, Cai J, Deshpande R, Zhou L, Hale MD, Lightwood DJ, Henry AJ, Popplewell AG, Moore AR, Robinson MK, Lacey DL, Simonet WS, Paszty C (2010) Two doses of sclerostin antibody in cynomolgus monkeys increases bone formation, bone mineral density, and bone strength. J Bone Miner Res 25:948–959
9. Padhi D, Allison M, Kivitz AJ, Gutierrez MJ, Stouch B, Wang C, Jang G (2014) Multiple doses of sclerostin antibody romosozumab in healthy men and postmenopausal women with low bone mass: a randomized, double-blind, placebo-controlled study. J Clin Pharmacol 54:168–178
10. Padhi D, Jang G, Stouch B, Fang L, Posvar E (2011) Single-dose, placebo-controlled, randomized study of AMG 785, a sclerostin monoclonal antibody. J Bone Miner Res 26:19–26
11. McClung MR, Grauer A, Boonen S, Bolognese MA, Brown JP, Diez-Perez A, Langdahl BL, Reginster JY, Zanchetta JR, Wasserman SM, Katz L, Maddox J, Yang YC, Libanati C, Bone HG (2014) Romosozumab in postmenopausal women with low bone mineral density. N Engl J Med 370:412–420

12. Cosman F, Crittenden DB, Adachi JD, Binkley N, Czerwinski E, Ferrari S, Hofbauer LC, Lau E, Lewiecki EM, Miyauchi A, Zerbini CA, Milmont CE, Chen L, Maddox J, Meisner PD, Libanati C, Grauer A (2016) Romosozumab treatment in postmenopausal women with osteoporosis. N Engl J Med 375:1532–1543

13. Cummings SR, Karpf DB, Harris F, Genant HK, Ensrud K, LaCroix AZ, Black DM (2002) Improvement in spine bone density and reduction in risk of vertebral fractures during treatment with antiresorptive drugs. Am J Med 112:281–289

14. Delmas PD, Li Z, Cooper C (2004) Relationship between changes in bone mineral density and fracture risk reduction with antiresorptive drugs: some issues with meta-analyses. J Bone Miner Res 19:330–337

15. Hernandez CJ, Keaveny TM (2006) A biomechanical perspective on bone quality. Bone 39:1173–1181

16. Bouxsein ML, Boyd SK, Christiansen BA, Guldberg RE, Jepsen KJ, Muller R (2010) Guidelines for assessment of bone microstructure in rodents using micro-computed tomography. J Bone Miner Res 25:1468–1486

17. Liu XS, Sajda P, Saha PK, Wehrli FW, Bevill G, Keaveny TM, Guo XE (2008) Complete volumetric decomposition of individual trabecular plates and rods and its morphological correlations with anisotropic elastic moduli in human trabecular bone. J Bone Miner Res 23:223–235

18. Zhou B, Liu XS, Wang J, Lu XL, Fields AJ, Guo XE (2014) Dependence of mechanical properties of trabecular bone on plate-rod microstructure determined by individual trabecula segmentation (ITS). J Biomech 47:702–708

19. Sanchez C, Deberg MA, Piccardi N, Msika P, Reginster JY, Henrotin YE (2005) Osteoblasts from the sclerotic subchondral bone downregulate aggrecan but upregulate metalloproteinases expression by chondrocytes. This effect is mimicked by interleukin-6, -1beta and oncostatin M pre-treated non-sclerotic osteoblasts. Osteoarthr Cartil 13:979–987

20. Liu XS, Stein EM, Zhou B, Zhang CA, Nickolas TL, Cohen A, Thomas V, McMahon DJ, Cosman F, Nieves J, Shane E, Guo XE (2012) Individual trabecula segmentation (ITS)-based morphological analyses and microfinite element analysis of HR-pQCT images discriminate postmenopausal fragility fractures independent of DXA measurements. J Bone Miner Res 27:263–272

21. Guo XE, Kim CH (2002) Mechanical consequence of trabecular bone loss and its treatment: a three-dimensional model simulation. Bone 30:404–411

22. Banse X, Devogelaer JP, Delloye C, Lafosse A, Holmyard D, Grynpas M (2003) Irreversible perforations in vertebral trabeculae? J Bone Miner Res 18:1247–1253

23. Banse X, Devogelaer JP, Holmyard D, Grynpas M (2005) Vertebral cancellous bone turn-over: microcallus and bridges in backscatter electron microscopy. Micron 36:710–714

24. Altman AR, Tseng WJ, de Bakker CM, Huh BK, Chandra A, Qin L, Liu XS (2014) A closer look at the immediate trabecula response to combined parathyroid hormone and alendronate treatment. Bone 61:149–157

25. Altman AR, de Bakker CM, Tseng WJ, Chandra A, Qin L, Liu XS (2015) Enhanced individual trabecular repair and its mechanical implications in parathyroid hormone and alendronate treated rat tibial bone. J Biomech Eng 137:10

26. Schulte FA, Lambers FM, Kuhn G, Muller R (2011) In vivo micro-computed tomography allows direct three-dimensional quantification of both bone formation and bone resorption parameters using time-lapsed imaging. Bone 48:433–442

27. Birkhold AI, Razi H, Duda GN, Weinkamer R, Checa S, Willie BM (2014) Mineralizing surface is the main target of mechanical stimulation independent of age: 3D dynamic in vivo morphometry. Bone 66:15–25

28. de Bakker CM, Altman AR, Tseng WJ, Tribble MB, Li C, Chandra A, Qin L, Liu XS (2015) muCT-based, in vivo dynamic bone histomorphometry allows 3D evaluation of the early responses of bone resorption and formation to PTH and alendronate combination therapy. Bone 73:198–207

29. Lambers FM, Schulte FA, Kuhn G, Webster DJ, Muller R (2011) Mouse tail vertebrae adapt to cyclic mechanical loading by increasing bone formation rate and decreasing bone resorption rate as shown by time-lapsed in vivo imaging of dynamic bone morphometry. Bone 49:1340–1350

30. de Jong JJ, Willems PC, Arts JJ, Bours SG, Brink PR, van Geel TA, Poeze M, Geusens PP, van Rietbergen B, van den Bergh JP (2014) Assessment of the healing process in distal radius fractures by high resolution peripheral quantitative computed tomography. Bone 64:65–74

31. Christen P, Ito K, Ellouz R, Boutroy S, Sornay-Rendu E, Chapurlat RD, van Rietbergen B (2014) Bone remodelling in humans is load-driven but not lazy. Nat Commun 5:4855

32. Ellouz R, Chapurlat R, van Rietbergen B, Christen P, Pialat JB, Boutroy S (2014) Challenges in longitudinal measurements with HR-pQCT: evaluation of a 3D registration method to improve bone microarchitecture and strength measurement reproducibility. Bone 63:147–157

33. Manhard MK, Nyman JS, Does MD (2016) Advances in imaging approaches to fracture risk evaluation. Transl Res. doi:10.1016/j.trsl.2016.09

34. Slyfield CR, Tkachenko EV, Wilson DL, Hernandez CJ (2012) Three-dimensional dynamic bone histomorphometry. J Bone Miner Res 27:486–495

35. Matheny JB, Slyfield CR, Tkachenko EV, Lin I, Ehlert KM, Tomlinson RE, Wilson DL, Hernandez CJ (2013) Anti-resorptive agents reduce the size of resorption cavities: a three-dimensional dynamic bone histomorphometry study. Bone 57:277–283

36. Slyfield CR Jr, Niemeyer KE, Tkachenko EV, Tomlinson RE, Steyer GG, Patthanacharoenphon C, Kazakia GJ, Wilson DL, Hernandez CJ (2009) Three-dimensional surface texture visualization of bone tissue through epifluorescence-based serial block face imaging. J Microsc 236:52–59

37. Cresswell EN, Goff MG, Nguyen TM, Lee WX, Hernandez CJ (2016) Spatial relationships between bone formation and mechanical stress within cancellous bone. J Biomech 49:222–228

38. Ominsky MS, Li C, Li X, Tan HL, Lee E, Barrero M, Asuncion FJ, Dwyer D, Han CY, Vlasseros F, Samadfam R, Jolette J, Smith SY, Stolina M, Lacey DL, Simonet WS, Paszty C, Li G, Ke HZ (2011) Inhibition of sclerostin by monoclonal antibody enhances bone healing and improves bone density and strength of nonfractured bones. J Bone Miner Res 26:1012–1021

39. Doube M, Klosowski MM, Arganda-Carreras I, Cordelieres FP, Dougherty RP, Jackson JS, Schmid B, Hutchinson JR, Shefelbine SJ (2010) BoneJ: free and extensible bone image analysis in ImageJ. Bone 47:1076–1079

40. Salmon PL, Ohlsson C, Shefelbine SJ, Doube M (2015) Structure model index does not measure rods and plates in trabecular bone. Front Endocrinol 6:1–10

41. Maquer G, Musy SN, Wandel J, Gross T, Zysset PK (2015) Bone volume fraction and fabric anisotropy are better determinants of trabecular bone stiffness than other morphological variables. J Bone Miner Res 30:1000–1008

42. Chavassieux P, Portero-Muzy N, Roux JP, Garnero P, Chapurlat R (2015) Are biochemical markers of bone turnover representative of bone histomorphometry in 370 postmenopausal women? J Clin Endocrinol Metab 100:4662–4668

43. Ross RD, Edwards LH, Acerbo AS, Ominsky MS, Virdi AS, Sena K, Miller LM, Sumner DR (2014) Bone matrix quality after sclerostin antibody treatment. J Bone Miner Res 29:1597–1607